Malaysian Journal of Chemistry, 2024, Vol. 26(3), 211-232
(Special Issue: *The International Conference on Advanced Materials & Sustainable Energy Technologies 2023*)

Co-Gasification of Palm Oil EFB and MSF for Renewable Hydrogen Production: A Conceptual Design and Simulation

Lim, J. J. Y.[1], Ching, S. W.[1], Tan, Y. Y.[1], Goh, Z. R.[1], Chang, S. W.[1], and Mohd, N.[1,2]*
[1]School of Energy and Chemical Engineering, Xiamen University Malaysia, 43900 Sepang, Selangor, Malaysia
[2]College of Chemistry and Chemical Engineering, Xiamen University, Xiamen 361005, Fujian, China
*Corresponding author (e-mail: noraini.mohd@xmu.edu.my)

Utilizing non-edible lignocellulosic biomass for second-generation biofuel production offers a promising solution to address agricultural and food waste accumulation. The objective of this study is to design a plant capable of producing biohydrogen and three other biofuels simultaneously. Palm-based empty fruit bunch and mesocarp fiber are chosen as feedstock for their cost-effectiveness, high production rate, and low moisture content. Feasibility is assessed through Aspen Plus simulation and process flow diagram (PFD) illustration. The designed PFD integrated sustainability principles spanning economic, social, and environmental dimensions such as the inclusion of flue gas treatment, the integration of a gas cyclone in the flue gas cleaning system and the adoption of a unified cooling water stream. Located in Kuantan, Pahang (3.8168 ˚N, 103.3317 ˚E), the designed plant successfully achieves a production capacity of 62.5 kt of 99 % purity renewable hydrogen annually with the potential cost of USD 12.40 per kg of output.

Keywords: Empty fruit bunch; hydrogen; conceptual plant design; process flow diagram; simulation

Received: January 2024; Accepted: February 2024

Second-generation biofuels, derived from perennial crops such as willow, eucalyptus, and silver grass, along with non-edible lignocellulosic biomass like citrus peel, barley straw, and corn stover, offer a sustainable solution. Emphasizing the utilization of non-edible lignocellulosic biomass can significantly mitigate the accumulation of agricultural and food waste. Operational costs for second-generation biofuels are projected to be substantially lower than those for first-generation counterparts, with raw material expenses comprising only 25–30 % of the total price of food crops [1-4].

As depicted in **Figure 1**, circular bioeconomy can be initiated gratifyingly by utilizing the second-generation biofuels, wherein the potential of biomass can be maximized through successive utilization over time. Wastes and residues can be further converted into value-added products by upcycling sustainable and resource-efficient biomass through integrated production chains. The implementation of circular bio-economy can enhance biomass conversion efficiency and the production of value-added commodities, while also generating new economic opportunities for rural communities and contributing to climate change mitigation. It is plausible that the circular bioeconomy will contribute to achieving sustainable development goal (SDG) 11, which advocates for sustainable urbanization [5, 6].

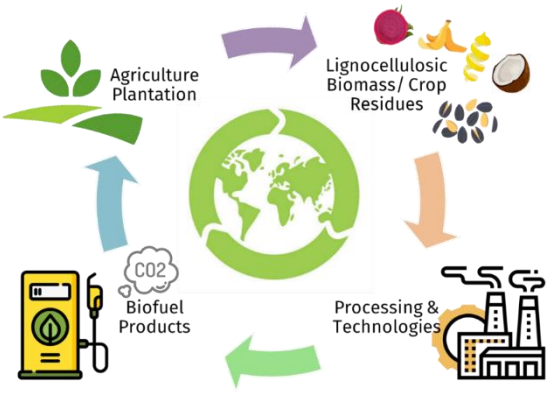

Figure 1. Circular Bioeconomy.

†Paper presented at the International Conference on Advanced Materials & Sustainable Energy Technologies 2023

Beyond its significance in attaining the SDGs, the escalating demand for biofuels including renewable hydrogen stems from various factors, including (i) the pursuit of clean and renewable energy sources, (ii) the promotion of carbon-neutral biofuels to enhance carbon sequestration and diminish greenhouse gas emissions, (iii) the generation of employment opportunities for local communities, (iv) the reduction of air pollution through the mitigation of agricultural crop residue accumulation and burning, and (v) the enhancement of national economic growth by decreasing dependence on imported hydrocarbons [7-9].

Leveraging the inherent qualities and advantages of second-generation biofuel, this study strives to design and construct a novel hydrogen production facility using a secondary-generation biofuel source capable of fulfilling worldwide demand. There are two research questions to be answered: (1) which process route is the best to produce biofuel, and (2) how to construct a sustainable conceptual design for renewable hydrogen production. Therefore, the objectives of this study are: (1) to select the best process routes for biofuel production, and (2) to construct a biofuels production plant that includes a production rate of more than 50 kt per year of renewable hydrogen. A feasibility study will be conducted on the best-chosen process route upon comparison of a minimum of three routes. Consequently, this investigation will concentrate on devising a plant capable of producing three biofuels through one process route.

CONCEPTUAL DESIGN

Process Route Selection

Various criteria were employed to evaluate different process pathways, as summarized in Table 1. The selection of the optimal process considered factors such as safety, environmental impact, and economic considerations. Economic aspects were further categorized into profit margin, operating costs, and biogas production yield.

Table 1. Process routes comparison.

Process routes	Anaerobic digestion	Pyrolysis	Co-gasification
Production yield	Biomethane: 82.22 % Bio-oil: 2.82 % Hydrochar: 0.576 %	Bio-oil: 45.75 % Bio-char: 29.05 % Bio-gas: 25.2 %	Bio-gas: 88.67 % Solid Residue: 5.67 % Ash: 2.15 % Bio-char: 0.54 %
Strengths	Optimum C/N ratio	Free of highly toxic throughput production Diverse biomass materials applicable	Costs effective Elevated energy efficiency Competitive quality with diesel
Weaknesses	Extensive consumption of energy High capex of electrolysis May cause undesired respiratory inflammation upon exposure [10, 11].	Require treatment to reduce the high concentration of CO in the produced gas. Fire and explosion hazards.	Relatively sensitive process, skill level required disposal of effluents (scrubbing water).
Environmental impact	Potential circumstance of soil and water related issue. May become source of pathogens.	Minimal greenhouse gasses emission.	Production of polyhalogenated organic compounds. Generation of chars and tars. Emission of toxic and heavy metals elements.
Scale	Commercial	Commercial	Pilot
Operating cost (USD M/year)	33.9	66.66	0.18
Profit margin (USD M/year)	1988.49	195	313.41

Table 2. Main characteristics of batch, semi-batch and continuous.

	Continuous	Batch	Semi-batch
Temperature	250 - 450 ℃	100 - 380 ℃	170 - 310 ℃
Pressure	23 – 100 MPa	0.1 – 22 MPa	10 – 20 MPa
Residence time	Millisecond-seconds	Minute - hours	Minutes
Equipment requirements	High	Low	Medium
Process control	High	Low	Medium

Co-gasification exhibited the highest yield in biogas production, indicating its capability to generate the most biogas from the same quantity of biomass raw material. Furthermore, among the proposed process pathways, co-gasification exhibited the lowest operational costs, implying its potential to maximize profits at a reduced expense. Anaerobic digestion showcased notably high profitability margins, encompassing profits from by-products. Consequently, when solely comparing profits derived from the primary product, hydrogen gas, the value is expected to be considerably lower. Hence, from an economic standpoint, co-gasification remains the most favorable option. Anaerobic digestion poses potential environmental risks by impacting soil and water quality and serving as a breeding ground for pathogens. In such scenarios, pyrolysis and co-gasification emerge as preferable alternatives since they both generate hydrogen gas and produce non-polluting solid carbon char from natural gas, with co-gasification releasing minimal carbon dioxide emissions. From a safety perspective, pyrolysis presents a substantial risk of fire and explosion attributed to the release of hydrocarbons. In contrast, co-gasification entails potential hazards related to the piping in the air separation unit (ASU), where leakage of liquid oxygen could lead to severe combustion. Thermal liquefaction necessitates preheaters to elevate the biomass slurry temperature, but there's a risk of overheating, potentially causing explosions and significant damage. During anaerobic digestion, the predominant components of biogas are methane and carbon dioxide. Mitigating methane leakage is crucial to prevent fire hazards, as methane can form explosive mixtures in the air, resulting in explosions.

PROCESS DESIGN AND SYNTHESIS

Level 1: Process Operating Mode

The initial step towards assessing economic potential involves identifying the input data, also referred to as design factors. These data points will primarily originate from the process mode employed in the study. Process modes can be classified into three main categories: batch, semi-batch, and continuous. Among these, continuous operation offers numerous advantages over batch and semi-batch modes, including the ability to consistently produce high-quality goods at lower capital costs and higher productivity rates. These benefits directly contribute to increased production profit margins. Additionally, continuous processes enable improved process control and monitoring, enhancing asset utilization. **Table 2** presents a comparative analysis of various operating modes.

Level 2: Input-output Structure of the Flowsheet

However, the second tier of the Douglas hierarchical process states the feed flow rate is perceived as the limited factor for the design variables, scrutinizing the input-output structure of the process flowsheet. The central focus of this study's input-output structure lies in the co-gasification of raw biomass feedstock, specifically empty fruit bunches (EFB) and mesocarp fiber (MSF), aimed at hydrogen production [12, 13]. It's imperative to emphasize that the economic evaluation of this study will solely consider its primary product: hydrogen. The complete mass balance for the proposed co-gasification process is depicted in **Figure 2**, in which $\dot{m}$ refers to the mass flow rate of each stream. As illustrated, 63,535.389 kg/h of water and 29,650 kg/h of EFB and MSF were inserted into the co-gasification reaction, resulting in an output of 7,000.672 kg/h of purified hydrogen throughput.

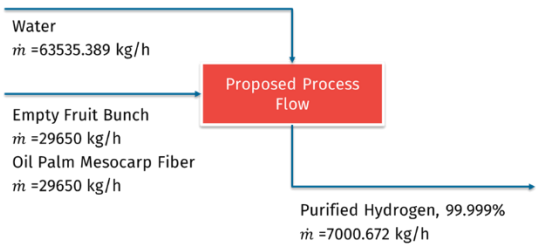

Figure 2. Overall mass balance in the process boundary.

Table 3. The price list of the involved materials.

Materials	Price (USD/kg)
Purified Hydrogen (99 %), H_2	12.5
Water	0.00019
Oil Palm Mesocarp Fiber	0.012
Empty Fruit Bunch	0.012

Table 4. Calculation summary of the economic potential.

Parameters	**Inlet**		**Outlet**	
Material	EFB	MSF	Water	H_2
Mass flow rate (kg/h)	29650	29650	63535	7000.7
kg/kg product	4.24	4.24	9.08	1
USD/kg	0.012	0.012	0.0002	12.5
EP (USD/kg Product)	**12.397**			

Understanding the cost of the raw materials, including water, hydrogen, EFB, and MSF, is essential for conducting the economic potential analysis, which is tabulated in **Table 3**.

As revealed in the equation below, the second tier of the economic potential mainly refers to the income generated by the process and the expense associated with the raw materials, whereby C indicates the cost and F indicates the molar ratio [14].

$$Revenue - Raw\ Material\ Cost = Economic\ Potential\ (Level\ 2)$$
$$f_{ep} = \sum C_P F_P - \sum C_R F_R \quad (1)$$

Therefore, the economic potential of the study can be computed as below:

$$f_{ep} = [(4.24 \times 0.012) + (0.00019 \times 9.08) + (12.5) \times (1) - (4.24 \times 0.012)]$$
$$f_{ep} = 12.397\ (USD/kg\ product)$$

Table 4 outlined the summary of the comprehensive economic potential calculation study, revealing that the process can be deemed profitable, whereas a general profit of USD 12.40 can be earned with the production of 1 kg hydrogen.

Level 3: Reactor Design and Reactor Network Synthesis.

The proposed co-gasification plant consists of four key phases, which include (1) the co-gasification process, (2) air separation process, (3) water gas shift reaction, and (4) hydrogen purification process. Among these, co-gasification stands out as the pivotal step, wherein biomass feedstock (EFB and MSF) is initially converted into hydrogen gas, the desired end product.

Concurrently, side products such as carbon monoxide are also generated during this phase. To enhance the overall production yield of hydrogen gas, it is advisable to employ the water gas shift reaction, which facilitates the conversion of produced carbon monoxide with steam into hydrogen and carbon dioxide.

Co-gasification Process

As depicted in **Figure 3**, pre-shredded EFB and MSF will undergo drying processes to reduce the moisture content of the biomass. Ensuring optimal gasification performance is crucial, as high biomass moisture content can significantly lower reaction temperatures and impede gasification reactions [15, 16]. Subsequently, the dried raw material will be transferred to the co-gasifier using a screw conveyor. Additionally, oxygen generated at the ASU will be introduced into the co-gasifier as a gasifying agent to facilitate the conversion of biomass into syngas.

In the co-gasifier, one of the reactions occurring is the pyrolysis of dried biomass materials, liberating char (carbon) and other volatile species that subsequently engage in a series of gasification processes [17]. Sikarwar, Zhao [18] delineate the biomass gasification process into three sequential reaction steps. During the primary reaction step, biomass material undergoes transformation into primary oxygenated vapors, liquid chemicals, water vapor, and carbon dioxide at temperatures below 500 °C. In the secondary stage, occurring between 700 and 850 °C, original liquid and vapor species are converted into products like tar, hydrogen, carbon dioxide, water vapor, gaseous olefins, phenolic and aromatic species, and carbon monoxide. These gaseous species facilitate various reactions including cracking, methanation, steam reformation, and water-gas shift. The tertiary stage, between 850 and 1000 °C, sees the formation of carbon dioxide, carbon monoxide, hydrogen, aromatic compounds, tar and water vapor. Moreover, Liao, Wu [19] documented that the presence of inorganic components in the biomass raw material facilitates the generation of ash during the gasification process. Fly ash and bottom ash primarily comprise oxides of aluminum, calcium, iron, and other metals, alongside residual char [19].

Decision 1: Reactor Performance

To determine the most suitable gasification technique, this study investigated fluidized bed, entrained flow, fixed bed, and spouted bed gasifiers, with the results presented in **Table 5**.The entrained flow gasifier, designed for gasifying finely refined coal, imposes restrictions on fuel particle size, rendering it unsuitable for fibrous biomass gasification, particularly MSF as recommended in the biomass feedstock [18, 21].

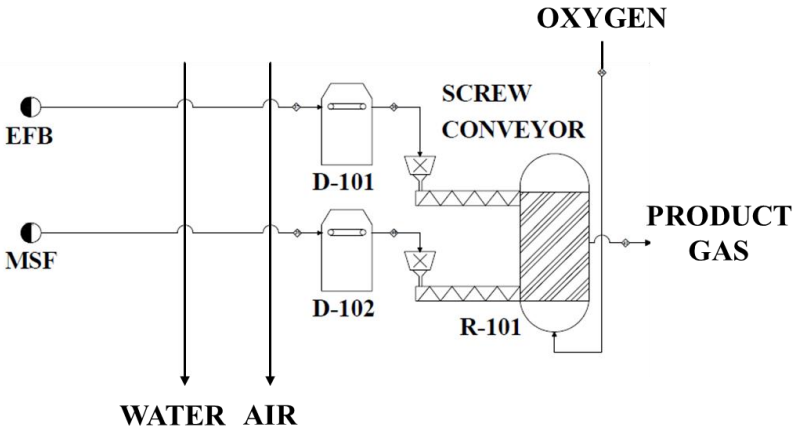

Figure 3. A schematic diagram of the co-gasification process unit: R-101 is co-gasifier; D-101 -102 are belt dryers.

Table 5. Comparison table for co-gasification reactor selection.

Parameter		Fluidized Bed	Entrained Flow	Fixed Bed	Spouted Bed
Process mode		Continuous	Continuous	Batch	Continuous
Particle size	(mm)	0.1 – 5	0.7	< 0.1	< 0.2
Temperature	(℃)	800-900	1200 - 1500	750	900 - 1000
Biogas production yield	(%)	60	72	60	70 - 80
Cost		Low	High	Low	Low
Operation		Simple	Complex	Simple	Complex
Limitations		Back mixing limit results in slow oxygen diffusion and biomass conversion rate	Fuel size restrictions	Fuel size and moisture content restrictions	Tar cracking reactions can be limited by the short residence time of the volatiles
References		[20]	[21]	[22]	[23]

Among the gasifiers, fixed bed gasifiers are widely used due to their simple construction, cost-effective operation, and minimal need for raw material pre-treatment. However, they are typically utilized in batch operations due to their limited capacity to handle large quantities of biomass [18, 22]. Consequently, for the proposed continuous process, fixed bed gasifiers are deemed unsuitable. In large-scale biomass gasification processes operating continuously, fluidized bed gasifiers are commonly employed. The circulating gasifying medium enhances heat and mass transfer between phases and can accommodate a wide range of biomass particle sizes while maintaining consistent temperature distribution within the gasifier bed. It possesses the capability to handle diverse biomass feedstocks. Furthermore, in comparison to fixed bed gasifiers, it demonstrates a relatively higher capacity for processing biomass [18]. An appropriate reactor choice for the proposed co-gasification process is the fluidized bed gasifier. Conversely, the conical spouted bed reactor (CSBR) has commonly been utilized for gasifying plastic waste or a fraction of biomass feedstock to address the defluidization issue encountered by the fluidized bed reactor (FBR). Herbaceous biomass feedstock with elevated Si, K, and Ca content may lead to the formation of viscous mixes, promoting particle agglomeration and hindering fluidization in FBR. Similarly, FBR experienced agglomeration and defluidization due to plastic melting. Hence, the application of high collisions and vigorous particle movement in CSBR has been identified as an effective approach to prevent bed defluidization caused by particle agglomeration [18, 24]. When gasifying a unique feedstock necessitating defluidization— which is not the case for the suggested biomass, EFB, and MSF- CSBR emerges as a preferable option. Compared to fixed bed and fluidized bed reactors, the spouted bed reactor features a more intricate design and operation, requiring multiple pumps, thereby escalating the initial system cost. Additionally, Sebastian and Paul [25] asserted that the primary drawback of spouted bed gasification is the brief residence time of volatiles, hindering tar-cracking reactions. Following the elimination of problematic choices, the fluidized bed gasifier stands out as the most suitable reactor for the proposed co-gasification process.

Decision 2: Reactor Operating Conditions

Table 6 presents the operational status of the gasifier. Sikarwar, Zhao [18] emphasizes that gasifier temperatures exceeding 800 °C can lead to a higher yield of gaseous products derived from carbon, volatile species, and high molecular weight hydrocarbons, hence favoring higher gasification temperatures. According to findings by Loha, Chatterjee [26], an increase in the temperature of biomass gasification results in higher production of carbon monoxide and hydrogen, while methane and carbon dioxide production decrease. Ding and He [17] observed similar trends and proposed that this phenomenon may be attributed to elevated temperatures enhancing the Boudouard reaction and steam reforming reaction [17]. Moreover, when the gasification temperature reaches approximately 900 °C, all processes tend to approach equilibrium, and the composition of the syngas produced tends to stabilize accordingly [17].

Table 6. Reactor operating condition for co-gasification.

Parameter	Value
Temperature	900 °C
Pressure	1 atm
Phase	▪ Solid phase: biomass particles ▪ Gas phase: oxygen and product gases
Catalyst	2.5 wt% Ni/Al_2O_3

Decision 3: Reactor Configuration

In the proposed process flow, the inlet and outlet streams and configuration of the gasifier are summarized in Table 7.

Water Gas Shift Reaction (WGSR)

The co-gasification process yields a variety of chemicals, such as carbon monoxide (CO), carbon dioxide (CO_2), hydrogen (H_2), and so on. The goal of the WGSR process is to boost the total yield of H_2 production by converting carbon monoxide and steam into carbon dioxide and hydrogen. It is said as follows [27]:

$$CO + H_2O \leftrightarrow CO_2 + H_2 \quad (2)$$

Table 7. Inlet and outlet streams in the gasifier system boundary.

Parameter	Value
EFB input flowrate	29650 kg/h
MSF input flowrate	29650 kg/h
Oxygen input flowrate	6383.51 kg/h
Gas outlet flowrate	65682.93 kg/h
Orientation	Vertical Fluidized Bed Reactor

Decision 1: Reactor Performance

The WGSR reactor, being a fixed bed reactor, employs a suitable catalyst primarily selected for its high conversion rate per unit weight, ease of construction, low capital and operational costs, and ability to operate under high pressure and temperature conditions. Due to the exothermic nature of the WGSR reaction, the production of H_2 is thermodynamically restricted at elevated temperatures in accordance to the Le Chatelier's principle. However, as per the Arrhenius equation, at higher temperatures, the reaction rate tends to increase, thereby enhancing CO conversion. To optimize H_2 production or CO conversion under such conditions, WGSR can be conducted in two temperature stages: a high-temperature step (HT-WGSR), typically ranging from 350 to 450 °C, employing high- temperature catalysts (HTCs); and a low-temperature step (LT-WGSR), typically ranging from 180 to 250 °C, utilizing low-temperature catalysts (LTCs) [28, 29]. A comparison table detailing the performance of various catalysts in WGSR is provided in Table 8. Renowning to the superior carbon monoxide conversion efficiency, copper-nickel on activated carbon (Cu-Ni/AC) was chosen as the catalyst for the WGSR process.

Table 8. Comparison table for WGSR catalyst selection.

Parameter	$Mn–Cr/TiO_2$	Cu/Fe_3O_4	Cu-Ni/AC	$Pt@CeO_2$/H-SBA-16
Temperature (℃)	320-420	275-400	200	360
CO conversion (%)	61.3	99.4	32	75
Pore size (nm)	6.67	3.1	6.5	N/A
Surface area (m^2/g)	1.5	415	773	N/A
References	[30]	[31]	[28]	[29]

Decision 2: Reactor Operating Conditions

Table 9. Operating conditions for WGSR reactor.

Parameter	Value
Temperature	360 °C
Pressure	1 bar
Phase	Gas phase: steam, carbon dioxide, hydrogen
Catalyst	Cu-Ni/AC catalyst

In this study, the WGSR process was proposed to occur at high temperature (HT-WGSR) environment, ranging from 350 to 450 ˚C, given the selection of the high-temperature catalyst, Cu-Ni/AC. The operating conditions of the WGSR reactor are summarized in **Table 9**.

Decision 3: Reactor Configuration

The inlet and outlet streams and orientation of the WGSR reactor are summarized in **Table** .

Table 10. Inlet and outlet streams and orientation of the WGSR reactor.

Parameter	Value
Gas input flowrate	65600.56 kg/h
Steam input flowrate	63535.39 kg/h
Gas outlet flowrate	129135.95 kg/h
Orientation	Vertical fixed bed reactor

Level 4: Separation System Synthesis

Decision 1: Types of Separators

The separation system is pivotal in the overall operation of the process plant. Implementing an appropriate separation procedure could potentially enhance the production yield of the final output in this study, which is pure hydrogen. The separators utilized in this investigation include a fluidized bed membrane reactor (FBMR) for hydrogen purification, a series of cryogenic distillation columns within the ASU responsible for oxygen separation and supply, and a cyclone separator located at the co-gasifier outlet, which is linked to an H_2S adsorber.

Decision 2: Sequencing of Separators

ASU: Cryogenic Distillation

The ASU, focusing on extracting oxygen from compressed air, is positioned at the upstream end of the process flow. Oxygen extracted from this unit would be transferred to the co-gasifier to serve as a reactant medium. Consequently, enhancing the purity of oxygen could enhance the production of biogas from the co-gasification process, which in turn would benefit the subsequent production of hydrogen downstream. In general, there are four major steps in the oxygen separation process: (1) air compression; (2) air cooling; (3) liquefaction; and (4) distillation. Several heat exchangers will be used to lower the temperature of the gas in preparation for the next step in the liquefaction process, as well as compressors powered by electric motors to compress a big volume of air to high pressures. The liquefied air would then be introduced into the distillation column to remove nitrogen.

Cyclone Separator

Gas cyclones are widely acknowledged as dust collectors extensively employed in industry. Acknowledging their high processing capacity and simple operating conditions, cyclones are deemed economically and technologically feasible for the gas purification process in the industries. The functionality of a cyclone priorly relies on the integration of centrifugal force to the suspended particles present in the swirling gas stream. In the context of removing palm oil fuel ash (POFA) generated during the gasification of EFB and MSF, a cyclone was positioned downstream of the co-gasification process. Remarkably, the collected POFA can be sold for additional revenue generation, with potential applications including dense membrane and asphalt production [32, 33].

H_2S Adsorption Column

Typically, the employed adsorption column serves the purpose of eliminating non-condensable H_2S, which can lead to pitting corrosion in pipelines and downstream equipment [34]. Additionally, the presence of carbon dioxide and oxygen in the working fluid may accelerate the corrosion process. It's worth mentioning that the H_2S adsorption process utilizes a packed bed reactor containing activated carbon [35, 36].

Table 11. Operating conditions of the distillation columns.

Equipment	Distillation Column 1		Distillation Column 2	
Stream	19	20	26	27
Temperature (℃)	-164.1	-164.1	-180.6	-184
Pressure (bar)	12	6.59	1.07	1.07
Mass flow rate (kg/h)	9374.59	19921.01	18092.96	11202.64
Nitrogen	7070.81	15025.48	10910.97	11185.32
Oxygen	2174.51	4620.83	6789.37	5.96

During the adsorption process, H_2S initially adheres to the surface of the adsorbent. Subsequently, it undergoes dissociation and dissolves, resulting in the production of water vapor [37, 38].

Hydrogen Purification Unit: Membrane Separation

An innovative component in the hydrogen purification process is the FBMR, which integrates the in-situ extraction of H_2 with methane dry reforming within a singular unit. By effectively reducing the mass transfer limitations of H_2 between the reaction bulk and the membrane wall, the design of this equipment becomes more applicable for industrial use [39, 40]. Notably, the FBMR has the capability to significantly enhance CH_4 conversion rates and increase H_2 production yields. This can be ascribed to its capacity to promptly remove H_2 from the reaction space upon completion of production, thereby boosting the availability of the reaction space and further facilitating the dry reforming process [41, 42]. It's worth mentioning that this study would utilize Al_2O_3 as the catalyst bed and integrate a flat sheet Pd-Cu alloy membrane into the system.

Decision 3: Operating Conditions

The operating conditions of each inlet stream with respect to the distillation column, cyclone and the FBMR was summarized in the following tables:

Table 12. Operating conditions of the cyclones.

Stream	50
Temperature (℃)	360
Pressure (atm)	1
Grade efficiency	90%
Particle size (for removal)	> 0.258 μm
Phase	Mix
Mass flow rate (kg/h)	129135.95
Methane	358.44
CO	4504.86
CO_2	82426.71
Hydrogen	7801.45
Nitrogen	387.53
Oxygen	0.000
Water	30748.69
Chlorine	182.79
Ash	2725.43

Level 5: Heat Integration

Pinch Analysis

Pinch technology takes into account all heat transfers within a large energy-consuming facility in an effort to reduce external heat transfers to or from the location. By improving the process's heat recovery and lowering the external utility, it may be possible to reduce energy consumption financially. This plant's earlier design called for the heating or cooling of a total of 14 streams, whereby “HOT” stream indicates the streams that require cooling whilst “COLD” streams refer to streams that require heating. The heating element has not received any work (W). Consequently, the heat load and the enthalpy change (ΔH) were equivalent (Q) [43].

$$\Delta H = Q + W \tag{3}$$

Enthalpy change formula:

$$\Delta H = mC_p\Delta T \tag{4}$$

With an acceptable temperature difference T_{min}, which was chosen as 10 K as advised by Linhoff March's application, the maximum amount of heat transmission could be done [44]. Shifted temperature (T_{shift}) was calculated by the equation below:

$$T_{shift} = T_{act} \pm \frac{\Delta T_{min}}{2} \tag{5}$$

Table 13. Operating conditions of the FBMR.

Stream	54
Temperature (°C)	400
Pressure (atm)	1.283
Hydrogen permeation recovery	90.5 %
CO_2 removal	99 %
Phase	Mix
Mass flow rate (kg/h)	126410.52
Methane	358.44
CO	4504.86
CO_2	82426.71
Hydrogen	7801.45
Nitrogen	387.53
Oxygen	0.000
Water	30748.69
Chlorine	182.79
Ash	0.000

The process streams data was noted as below.

Following the completion of pinch analysis using the problem table method, it was determined that a minimum hot utility of approximately 26825 kW and a minimum cold utility of about 9319 kW are required. The cold pinch temperature is identified at 25 °C,

while the hot pinch temperature is noted at 45 °C as indicated in **Table** . The pinch arises at an interval temperature of 35 °C, indicating that no heat transfer is possible across this boundary. The potential heat exchange between the hot and cold streams were revealed perspicuously by both cold and hot composite curves as delineated in **Figure 4**. Significantly, the hot composite curve (red curve) aligns with the cold composite curve (blue curve), stipulating the presence of heat transfer from hot to cold stream upon heat recovery. The pinch occurs at the point where the two curves are closest to each other.

Table 14. Process stream data of the plant.

Stream name	Inlet stream	Outlet stream	Supply temperature (°C)	Target temperature (°C)	Mass flow rate (kg/h)	Net duty (kW)	Heat capacity (kW/K)
HOT 1	S12	S13	151.65	30.00	28695.60	-981.77	8.07
HOT 2	S14	S15	91.13	30.00	28695.60	-493.30	8.07
HOT 3	S38	S25	142.87	-164.10	9182.59	-1219.80	3.97
HOT 4	S17	S26	30.00	-164.10	19513.01	-1102.87	5.68
HOT 5	SUB28	S30	-179.00	-184.00	10973.20	-33.25	6.65
HOT 6	S29	S31	-175.42	-180.60	17722.40	-50.17	9.68
HOT 7	SUB42	S42	900.00	360.00	65469.82	-19992.86	37.02
HOT 8	S48	STORAGE	400.00	-251.95	7138.49	-20133.45	30.88
COLD 1	S21	S37	-182.25	27.00	6252.77	697.09	3.33
COLD 2	S35	S36	-194.75	29.25	22442.83	1448.05	6.46
COLD 3	S46	S47	360.00	400.00	126279.78	2938.18	73.45
COLD 4	WATER		25.00	100.00	3526.75	47405.42	632.07
COLD 5		S43	100.00	360.00	3526.75	9025.16	34.71

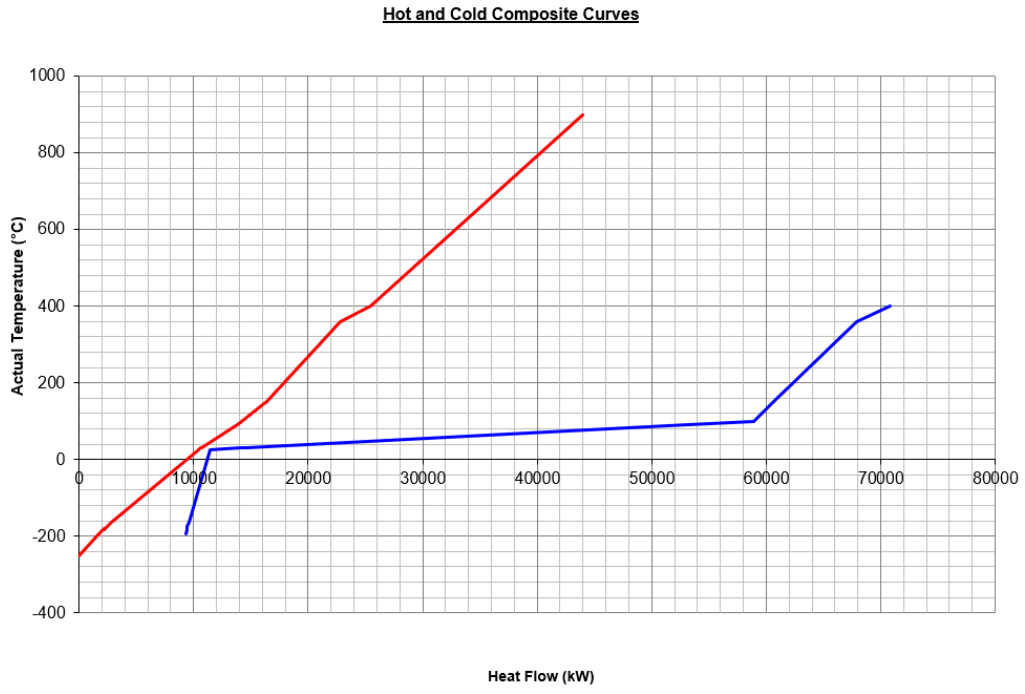

Figure 4. Hot and cold composite curves for the pinch analysis.

In **Figure 5**, a grand composite curve (GCC) was generated to illustrate the surplus heat within each interval. To satisfy the demands of cold streams, heat is transferred to lower temperature intervals. In some cases where the demand for cold streams surpasses the heat transferred, external heat utility becomes pivotal to boost the cold stream temperature to the desired level. In fact, the detailed information of the minimum cold and hot utility required for the process was furnished comprehensively by the GCC illustrated. The values for minimum cold and hot utility obtained from the GCC align with those acquired through the problem table method, totaling 26,825 kW for minimum hot utility and 9,319 kW for minimum cold utility.

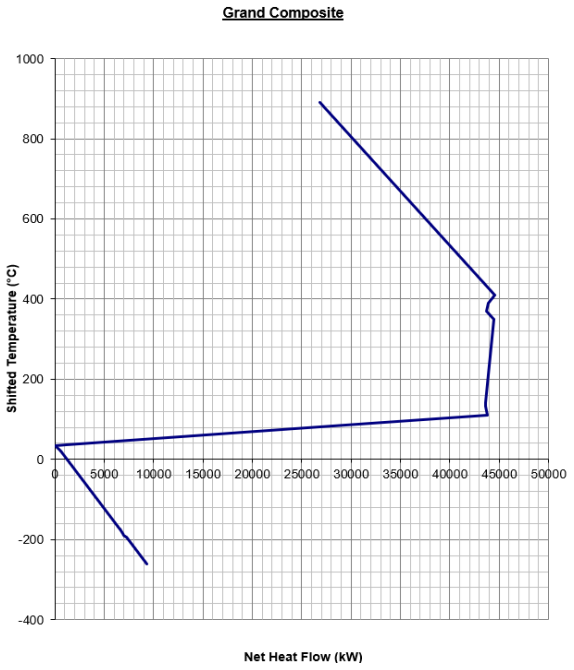

Figure 5. Grand composite curve.

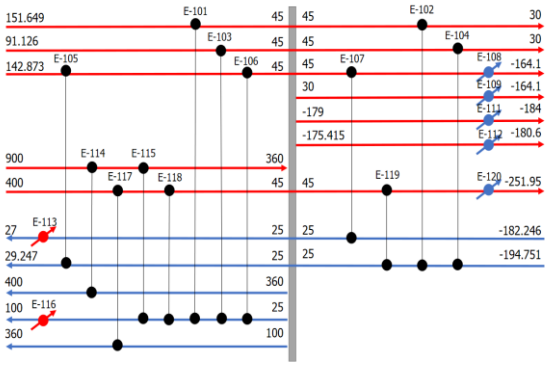

Figure 6. HEN design.

Figure 6 illustrated the golden rule-connected heat exchanger network (HEN) grid diagram constructed in this study, whereby no external heating ($Cp_{hot} > Cp_{cold}$), no external cooling ($Cp_{hot} < Cp_{cold}$) and no process heat exchangers can be observed below, above and across the pinch, respectively.

At the pinch point, COLD 4 stream required 47405.4 kW of heat to raise its temperature from 25 °C to 100 °C. HOT 1, HOT 2, HOT 3, HOT 7, and HOT 8 were connected to COLD 4 stream to provide a total of 20587.17 kW of heat, leaving a remaining heat requirement of 26818.23 kW from external heat sources to reach the target temperature. COLD 5 required 9025.12 kW of heat to increase its temperature from 100 °C to 360 °C. HOT 8 alone supplied the required 9025.12 kW of heat, fully enabling COLD 5 stream to achieve the target temperature. HOT 3 transferred 27.4568 kW to COLD 2, while HOT 7 contributed 2938.16 kW to COLD 3. Regarding the hot streams, HOT 1, HOT 2, HOT 3, HOT 7, and HOT 8 released approximately 860.6574 kW, 372.2368 kW, 388.9473 kW, 19992.96 kW, and 10963.11 kW, respectively, to the cold streams.

Minimizing the requirement for external cooling and heating systems can be pivotal in limiting the plant's carbon emissions and operational expenses. Therein, to achieve such an ideal scenario, it is critical to have a complete diffusion of heat from the hot streams to the cold streams. In this study, stream COLD 2 was connected to numerous hot streams, including HOT 1, HOT 2, and HOT 8, to obtain a total heat of 1420.69 kW. Meanwhile, stream COLD 1 was linked to stream HOT 3 to absorb 690.3364 kW of heat. Throughout the heating and cooling system design, it should be highlighted that an external cooling source is necessary to reduce the temperature of streams HOT 4, HOT 5, and HOT 6, as they were not linked to any cold stream for heat release.

Minimizing the requirement for external cooling and heating systems can be pivotal in limiting the plant's carbon emissions and operational expenses. Therein, to achieve such an ideal scenario, it is critical to have a complete diffusion of heat from the hot streams to the cold streams. In this study, stream COLD 2 was connected to numerous hot streams, including HOT 1, HOT 2, and HOT 8, to obtain a total heat of 1420.69 kW. Meanwhile, stream COLD 1 was linked to stream HOT 3 to absorb 690.3364 kW of heat. Throughout the heating and cooling system design, it should be highlighted that an external cooling source is necessary to reduce the temperature of streams HOT 4, HOT 5, and HOT 6, as they were not linked to any cold stream for heat release.

Table 15. Problem table and Cascade.

Shift Temperature	Interval	$T_{(i+1)}$-T_i	mCp_{net}	dH		Infeasible Cascade	Feasible Cascade
°C		°C	kW/K	kW			
890						▼ 0	▼ 26825
	1	480	37.0238	########	surplus	17771.4	17771.4
410						▼ 17771	▼ 44597
	2	20	-36.4306	-728.6111	deman	-728.61	-728.611
390						▼ 17043	▼ 43868
	3	20	-5.5487	-110.9732	deman	-110.97	-110.973
370						▼ 16932	▼ 43757
	4	20	33.1936	663.8711	surplus	663.871	663.871
350						▼ 17596	▼ 44421
	5	208.351	-3.8303	-798.0396	deman	-798.04	-798.04
141.649						▼ 16798	▼ 43623
	6	8.776	4.2402	37.2122	surplus	37.2122	37.2122
132.873						▼ 16835	▼ 43660
	7	22.873	8.2139	187.876	surplus	187.876	187.876
110						▼ 17023	▼ 43848
	8	28.874	-589.1463	########	deman	-17011	-17011
81.126						▼ 11.759	▼ 26837
	9	41.879	-581.076	########	deman	-24335	-24334.9
39.247						▼ -24323	▼ 2502
	10	2.247	-587.5406	########	deman	-1320.2	-1320.2
37						▼ -25643	▼ 1182
	11	2	-590.872	-1181.744	deman	-1181.7	-1181.74
35						PINCH ▼ -26825	▼ 0
	12	15	41.2003	618.0045	surplus	618.004	618.004
20						▼ -26207	▼ 618
	13	192.246	30.7415	5909.9266	surplus	5909.93	5909.93
-172.246						▼ -20297	▼ 6528
	14	1.854	34.0729	63.1712	surplus	63.1712	63.1712
-174.1						▼ -20234	▼ 6591
	15	10.651	24.4173	260.0691	surplus	260.069	260.069
-184.751						▼ -19974	▼ 6851
	16	0.664	30.8819	20.5056	surplus	20.5056	20.5056
-185.415						▼ -19953	▼ 6872
	17	3.585	40.5585	145.4021	surplus	145.402	145.402
-189						▼ -19808	▼ 7017
	18	1.6	47.2075	75.532	surplus	75.532	75.532
-190.6						▼ -19732	▼ 7093
	19	3.4	37.5309	127.6051	surplus	127.605	127.605
-194						▼ -19605	▼ 7220
	20	67.95	30.8819	2098.4248	surplus	2098.42	2098.42
-261.95						▼ -17506	▼ 9319

Table 16. Utility comparison before and after heat integration.

Utility	Before (kW)	After (kW)	Energy saved (%)
Cold	61513.902	9319	84.85
Hot	44007.472	26825	39.04
Total	105521.374	36144	65.75

Following the completion of HEN matching, it was observed that COLD 1, COLD 4, HOT 3, HOT 4, HOT 5, HOT 6, and HOT 8 failed to reach the desired temperature, indicating the necessity for external heating or cooling sources. The total hot utility required amounts to approximately 26825 kW, while the cooling utility needed is around 9319 kW. As indicated in **Table** , the energy requirement post heat integration has successfully decreased by approximately 66 %, suggesting the potential for achieving a more sustainable plant operation post-integration.

PROCESS FLOW DIAGRAM

Aspen Plus Simulation

Properties Setup

The main component present in this simulation setup comprises EFB, MSF, carbon graphite (C), carbon monoxide (CO), carbon dioxide (CO_2), ethylene (C_2H4), ethane (C_2H_6), methane (CH_4), nitrogen (N_2), oxygen (O_2), hydrogen (H_2), hydrogen sulfide (H_2S), water, sulfur (S), chlorine (Cl_2), ash, and argon (Ar). Ascribing to the heterogenous nature of EFB, MSF, and ash, they were designated as non-conventional components [45], while C and S were categorized as solid types. This simulation of the co-gasification process emphasizes the utilization of the Peng-Robinson (PENG-ROB) method, due to its superior capability in determining the enthalpy of fluid mixtures. Specifically, the volume-translated Peng-Robinson Equation of State, known as one of the most popular cubic models globally, enables reliable estimations of physical and chemical exergy in both liquid and gas phases across all streams [46].

Renowning the ability of the PENG-ROB approach in accommodating the actual gases and non-polar compounds like ethylene and ethane, the primary constituents of the proposed hydrogen production process, it is particularly suitable for the current study's simulation [47]. Enthalpy and density computations for EFB, MSF, and ash are conducted using built-in models known as "HCOALGEN" and "DCOALIGT" [45]. The HCOALGEN model necessitates proximate, sulfur, and ultimate analysis results to compute the enthalpy of non-conventional components, whereas the DCOALIGT model requires only sulfur and ultimate analysis results to determine the density of these components [48]. HCOALGEN incorporates various empirical correlations such as heat capacity, heat of combustion, and heat of formation.

Co-gasification Simulation Setup

Throughout the simulation process, various assumptions were made, as outlined below [49]:

1) The inlet mass flow rate of both raw biomass material was assumed to be 1 to 1 ratio.

2) Nitrogen and ashes were assumed to be inert.

3) Tar and char were presumed to be carbon graphite (C) throughout the simulation.

4) The devolatilization of biomass was considered instantaneous, and volatile products primarily consisted of H_2, CO, CO_2, CH_4, and H_2O.

5) All the reactions involved were assumed to reach equilibrium, except for the WGSR.

6) Reaction kinetics were not considered during the simulation.

7) The process was assumed to be isothermal and operate in steady-state and zero-dimensional.

8) Negligible heat loss was taken into account in this process.

Inlet Conditions

EFB (S1) and MSF (S6) were defined as the primary inlet streams of the co-gasification process, whereas the specifications and components are summarized in **Table 17**.

Table 17. Chemical Properties of EFB and MSF [52].

Component ID	EFB (S1)	MSF (S6)
Mass flow (kg/h)	29650	29650
Temperature (°C)	25	25
Pressure (bar)	1	1
Attribute ID	**PROXANAL (%)**	
Moisture	14.4	12.1
FC (fixed carbon)	8.8	8.1
VM (volatile matter)	86.1	86.4
ASH	5.07	5.52
Attribute ID	**ULTANAL (%)**	
Ash	5.07	5.52
C	43.8	52.1
H	5.8	7.2
N	0.5	1
Cl	0.33	0.38
S	0.1	0.2
O	44.4	33.6
Attribute ID	**SULFANAL (%)**	
PYRITIC	0	0
SULFATE	0	0
ORGANIC	0	0

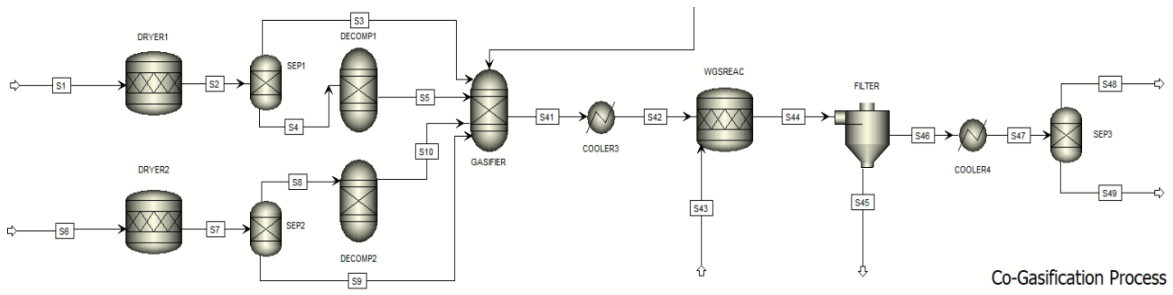

Figure 7. Process flow sheet for co-gasification process in ASPEN

Co-gasification Process Route in Aspen Simulation

Dryers (DRYER1 & DRYER2)

S1 and S6 underwent the DRYER 1 (100 ℃, 1 bar) and DRYER 2 (100 ℃, 1 bar) respectively, to dry up and generate water vapor. Both DRYERs defined in this simulation mainly operates using Rstoic, whereby S2 and S7 indicates the outlet stream from DRYER 1 and DRYER 2, respectively.

Separators (SEP1 & SEP2)

In the boundaries of both DRYERs, stream S2 and S7 were proceeded to different separators (SEP1 and SEP2) to separate water. In the first separator (SEP 1), a split faction of 1 was defined for EFB and water in the S4 and S3 outlet stream, respectively. Whilst, similar setup was defined in the second separator (SEP 2), whereby a split fraction of 1 was defined for MSF and water in the S8 and S9 outlet streams.

To drive the pyrolysis process and urge the formation of conventional chemicals from biomass, as well as to facilitate the involvement of EFB and MSF in phase or chemical equilibrium calculations, dry EFB (S4) and dry MSF (S8) were introduced into the decomposer units (DECOMP1 and DECOMP2) [45]. As elevated process temperature hinders char generation, the pyrolysis process was conducted at 1050 °C and 24 bar [51, 52].

Decomposers (DECOMP1 & DECOMP2)

RYield was employed in DECOMPs. When there's uncertainty regarding reaction kinetics and stoichiometry, RYield block can be utilized to provide yield distribution data. This approach was adopted to specify the yield distribution vector based on the final analysis of the EFB and MSF. Additionally, alongside the separated water in the separators, the output streams from DECOMP1 (S5) and DECOMP2 (S10) were simultaneously introduced into the GASIFIER.

Gasifier (GASIFIER)

S5 and S10 originating from the decomposers, along with S3 and S9 from the separators, and S37 from the ASU unit, constituted the five streams amalgamated and introduced into the GASIFIER. The outlet stream of the GASIFIER was denoted as S41. Calculation options included phase equilibrium and chemical equilibrium, with settings established at one bar of pressure and nine hundred degrees Celsius. Utilizing the RGIBBS reactor model, gasification reactions within the gasifier were simulated by minimizing the system's Gibbs free energy, allowing for the evaluation of both phase and chemical equilibrium [53]. This RGIBBS model facilitated the prediction of the equilibrium composition of the generated syngas, treating each component as a finished product. According to Ding et al., when the gasification temperature reaches approximately 900 °C, all processes tend to approach equilibrium, and the syngas produced reaches a stable state. Additionally, both the overall energy efficiency (OEE) and the cold gas efficiency (CGE) attain their optimal values at this temperature [17].

Cooler (COOLER3)

S41 was brought into COOLER3. In order to continue with the WGSR, COOLER3 was configured to operate at 360 °C and 0 bar, lowering the stream temperature from 900 °C to 360 °C. S42 was COOLER3's outlet.

Water Gas Shift Reactor (WGSREAC)

S42 was directed into the WGSREAC to facilitate a WGSR, aimed at consuming CO and generating more H_2, as H_2 was the desired product. The WGSREAC operated at 360 °C and 1 bar pressure. While higher pressure could potentially enhance CO conversion, its impact was minimal, almost negligible, given the absence of significant changes in mole numbers from reactants to products, rendering the reaction pressure-independent. Hence, the operating pressure could be set lower without substantially affecting hydrogen production, which could also help reduce operating costs [54]. Le Chatelier's principle suggests that as reaction temperature rises, the production of hydrogen decreases [55]. Therefore, to achieve a viable amount of H_2 and ensure an acceptable CO conversion, the WGSREAC was configured at 360 °C. The reaction involved the interaction of S43, a pure water inlet stream, with CO. For optimal H_2 production, the mole flow rate of S43 needed to be set at a minimum of 2010.93 kmol/hr to ensure complete reaction with the CO. The output stream from the WGSREAC was denoted as S44.

Filter (FILTER)

Modeled by the Split function in ASPEN, all the ash in stream S44 can be removed and collected in stream S45, while the remaining component present in stream S46 was proceeded for further process. Notably, a split fraction of NC was defined as 1 in S45, while the rest remained at 0.

Cooler (COOLER4)

In order to proceed the separation process, stream S46 was directed to COOLER4 to reduce the temperature from 360 ℃ to 150 ℃, while the outlet stream was defined as S47.

Separator (SEP3)

S47 was added to SEP3 in order to separate H_2 from CO_2 and purify the H_2 product. The H_2/CO_2 membrane separation process was modelled using SEP for the metallic membrane separator. 95 % of the H_2 permeate and 99 % of the CO_2 residual were recovered [56]. In S48, the split fractions of H_2 and CO_2 were set to 0.905 and 0.001, respectively, with the remaining value being 0. S48, the top SEP3 output stream, represents the product stream in this process overall, whereas S49, the bottom SEP3 outlet stream, represents the by-product stream.

Table 18. Simulation result in Aspen Plus.

		EFB inlet	MSF inlet	Product stream	By-product stream
	Units	**S1**	**S6**	**S48**	**S49**
Mass flows	**kg/hr**	**29650**	**29650**	**7138.49**	**119224**
ETHYL-01	kg/hr	0	0	0	0.0563
ETHAN-01	kg/hr	0	0	0	0.0062
METHA-01	kg/hr	0	0	0	400.351
CO	kg/hr	0	0	0	4504.48
CO2	kg/hr	0	0	82.3123	82230
HYDRO-01	kg/hr	0	0	7056.17	740.703
H2S	kg/hr	0	0	0	82.3776
NITRO-01	kg/hr	0	0	0	387.526
OXYGE-01	kg/hr	0	0	0	0
WATEREFB	kg/hr	0	0	0	30695.4
EFB	kg/hr	29650		0	0
MSF	kg/hr	0	29650	0	0
C	kg/hr	0	0	0	0
S	kg/hr	0	0	0	0
CHLOR-01	kg/hr	0	0	0	182.792
ASH	kg/hr	0	0	0	0
ARGON	kg/hr	0	0	0	0

Simulation Result

S48 is the main product stream of the co-gasification process, whereby 7138.49 kg/h (6.2576×10^7 kg/year) mass flow rate of H_2 with 98.8 % purity can be observed. According to this outcome, it can be deciphered that 29650 kg/h of the EFB and MSF are required to reach the target product capacity, which is 6.25×10^7 kg/year. **Table 18** depicted the simulation result obtained from Aspen Plus. O_2, and 0.01 mol% Ar underwent compression with a mass flow rate of 28695.6 kg/h, a temperature of 25 °C, and a pressure of 1.01 bar [57], whereas the cooling water stream (S18) of ASU comprises a mass flow rate of 160000 kg/h, at the temperature of 20 °C and 1.01 bar pressure.

Air Separation Unit (ASU) in Aspen Simulation

As described by Querol et al. [57], the primary inlet stream of ASU was air (S11), which mainly consists of 0.78 mol% N_2, 0.21 mol%. Facilitated by the cooling water stream (S18) in the heat exchangers (HEX1, HEX2), the intermittent cooling expedites the pressurization of the air inlet stream (S11) through multiple stages of compressors (COMP1, COMP2). Subsequently, the air stream (S15) was divided into two streams (S16, S17) through SPLITER1, whereas the latter (S17) was directed to the main heat exchanger (MULH) to experience a substantial temperature reduction before entering the high-pressure distillation column DC1. In the meantime, both product streams (S21 and S22) were warmed in the main heat exchanger (MULH), exchanging heat with streams S17 and S20 [57]. Conversely, the stream S16 underwent second cycle of pressurization and cooling process in COMP3 and HEX3, simultaneously before entering the MULH for external cooling. Subsequently, the cooled stream was further introduced into the 36-stages-high-pressure distillation column DC1 after experiencing expansion in VALVE1. Two streams comprising high purity of nitrogen (S28) and oxygen (S29) were produced and directed to individual cooling (COOLER1, COOLER2) and pressure adjustment (VALVE2, VALVE3). Subsequently, these streams were directed to a 70 stages of low-pressure column DC2. The as-produced oxygen-enriched stream (S34) was then pressurized to the desired pressure in liquid form using PUMP2. Parallelly, the nitrogen-rich stream (S35) underwent a temperature increase in a heat exchanger (HEX4). In the meantime, the oxygen stream, S37, was directed to the gasifier for syngas production. On the other hand, the nitrogen stream, S36, could undergo additional processing to generate marketable products such as liquid nitrogen or ammonia, among others. **Table** outlined the process para-meters for involved units in the ASU simulation.

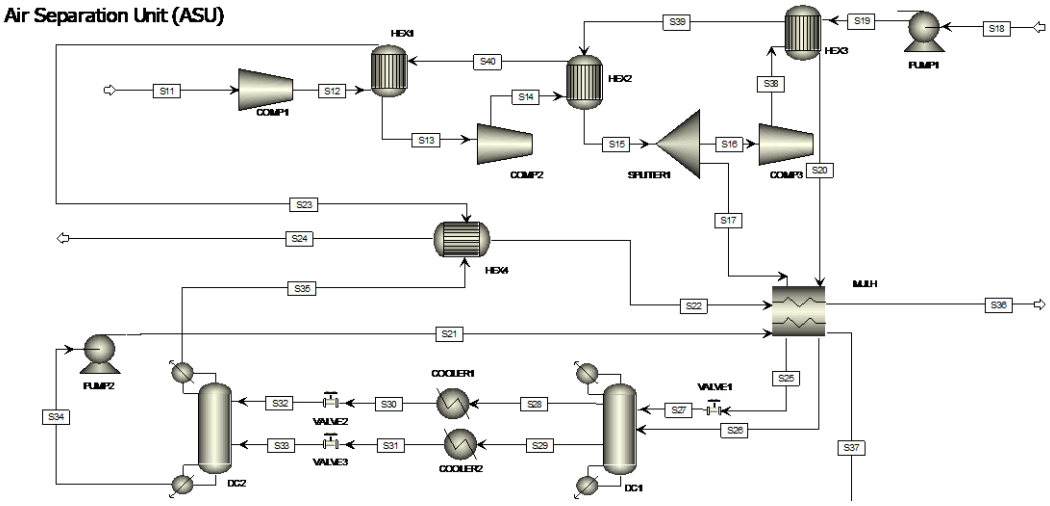

Figure 8. Process flow sheet for co-gasification process in ASPEN.

Table 19. Input specifications for each unit in ASU simulation.

Unit	**Specifications**	
Distillation column	DC1	Number of stages: 36 Condenser: Partial-Vapour Reflux ratio: 1.5 Feed streams: Stage 18 (Above-Stage) Product streams: S28 – Stage 1 (Vapor); S29 – Stage 36 (Liquid) Condenser pressure: 5.01 bar
	DC2	Number of stages: 70 Condenser: Partial-vapour Reflux ratio: 3 Feed streams: Stage 35 (On-Stage) Product streams: S34 – Stage 70 (Liquid); S35 – Stage 1 (Vapor) Condenser pressure: 1.06 bar
Heat exchanger		Counter current flow
	HEX1	Hot stream outlet temperature: 30 °C
	HEX2	Hot stream outlet temperature: 30 °C
	HEX3	Hot stream outlet temperature: 24.6 °C
	HEX4	Cold stream outlet temperature: -175 °C
	MULH	Inlet stream: S20 / S17 / S21 / S22 Exchanger side: HOT / HOT / COLD / COLD Outlet stream: S25 / S26 / S37 / S36 Temperature (°C): -164.1 / -164.1 / 27 Pressure (bar): 12 / 6.59 / 4.7
Compressor		Isentropic compressor
	COMP1	Discharge pressure: 2.58 bar
	COMP2	Pressure increase: 1.57 bar
	COMP3	Pressure increase: 5.41 bar
Pump	PUMP1	Discharge pressure: 3 bar
	PUMP2	Discharge pressure: 4.7 bar
Splitter	SPLITTER	Stream: S17 Split fraction: 0.68
Cooler	COOLER1	Temperature: -184 °C Pressure: 5.07 bar
	COOLER2	Temperature: -180.6 °C Pressure: 6.59 bar
Valve		Adiabatic flash for specified outlet pressure
	VALVE1	Outlet pressure: 6.59 bar
	VALVE2	Outlet pressure: 1.06 bar
	VALVE3	Outlet pressure: 1.06 bar

Table 20. Overall mass balance deviation between Excel calculation and ASPEN simulation.

Stream	Excel	Aspen	% Deviation	Stream	Excel	Aspen	% Deviation
1	29650.00	29650.00	0.00	**26**	19513.01	19513.01	0.00
2	29650.00	29649.35	0.00	**27**	9182.59	9182.59	0.00
3	4269.60	4268.95	0.02	**28**	10973.00	10973.20	0.00
4	25380.40	25380.40	0.00	**29**	17722.60	17722.40	0.00
5	25380.40	25380.40	0.00	**30**	10973.00	10973.20	0.00
6	29650.00	29650.00	0.00	**31**	17722.60	17722.40	0.00
7	29650.00	29650.00	0.00	**32**	10973.00	10973.00	0.00
8	26062.35	26062.35	0.00	**33**	17722.60	17722.40	0.00
9	3587.65	3587.10	0.02	**34**	6256.75	6252.77	0.06
10	26062.35	26062.35	0.00	**35**	22438.85	22442.83	0.02
11	28695.60	28695.60	0.00	**36**	22438.85	22442.83	0.02
12	28695.60	28695.60	0.00	**37**	6252.77	6252.77	0.00
13	28695.60	28695.60	0.00	**38**	9182.59	9182.59	0.00
14	28695.60	28695.60	0.00	**39**	160000.00	160000.00	0.00
15	28695.60	28695.60	0.00	**40**	160000.00	160000.00	0.00
16	9182.59	9182.59	0.00	**41**	68682.73	65552.19	4.56
17	19513.01	19513.01	0.00	**42**	68682.73	65552.19	4.56
18	160000.00	160000.00	0.00	**43**	63535.39	63535.39	0.00
19	160000.00	160000.00	0.00	**44**	128887.28	129087.58	0.16
20	9182.59	9182.59	0.00	**45**	2725.43	2725.43	0.00
21	6256.75	6252.77	0.06	**46**	126161.85	126362.15	0.16
22	22438.85	22442.83	0.02	**47**	126161.85	126362.15	0.16
23	160000.00	160000.00	0.00	**48**	7000.67	7138.49	1.93
24	160000.00	160000.00	0.00	**49**	119161.18	119223.67	0.00
25	9182.59	9182.59	0.00				

Table 20 reveals that the overall mass balance deviation ranges from 0.00 % to 4.78 %, whereas the highest deviation occurs in the co-gasification product stream. This disparity can be elucidated by the existence of differences between the assumptions made in manual calculation and ASPEN simulation within the co-gasification system boundary. Particularly, the specific mechanism that occurs within the RGIBBS block in the ASPEN simulation remains unclear, whereas the exact chemical reactions occurred was not realized. Hence, a high deviation reaching 4.78 % was obtained in the calculation outcome.

Throughout the development of the hydrogen production system, the computation of the mass balance within the co-gasification reaction system boundary was conducted according to the as-outlined chemical reactions. As summarized in **Table 21**, it should be highlighted that only minimal deviation was realized between the ASPEN and manual simulation with the assumption of 100 % carbon fractional conversion.

Table 21. Chemical reactions involved in the co-gasification process [17].

ID	Chemical Reaction	Reaction Name
R1	$C + O_2 \rightarrow CO_2$	Combustion
R2	$C + 0.5O_2 \rightarrow CO$	Partial Oxidation
R3	$C + CO_2 \rightarrow 2CO$	Boudouard
R4	$C + H_2O \rightarrow CO + H_2$	Steam Reforming
R5	$C + 2H_2 \rightarrow CH_4$	Methanation
R6	$H_2 + 0.5O_2 \rightarrow H_2O$	H_2 Oxidation
R7	$CO + 0.5O_2 \rightarrow CO_2$	CO combustion
R8	$CO + H_2O \rightarrow CO_2 + H_2$	Water Gas Shift
R9	$CH_4 + H_2O \rightarrow CO + 3H_2$	Methane-steam reforming
R10	$CH_4 + CO_2 \rightarrow 2CO + 2H_2$	Methane-CO_2 reforming

The estimation of char and tar through a thermodynamic equilibrium model can be complicated due to the non-equilibrium properties of tar. Therein, this study exempted the formation of tar and char throughout the manual calculation of the co-gasification process [58]. By employing these assumptions, a deemed acceptable final mass balance deviation of 4.56 % between ASPEN and manual calculation was resulted.

Analogous computations were performed for the WGSR within the co-downstream gasifier's operation. The redox type reaction known as the WGSR can be summed up by the following equation [59]:

$$CO + H_2O \rightarrow CO_2 + H_2 \quad (6)$$

In actuality, the manual mass balance calculation assumed a fractional conversion of 92 % CO, which was consistent with the ASPEN simulation [54]. After using the previously indicated fractional conversion and assumptions, the final mass balance divergence between the ASPEN simulation and manual calculation was found to be 0.16 %, which is considered acceptable.

Process Flow Diagram

The present study proposes the co-gasification of MSF and EFB to produce hydrogen. As depicted in **Figure 9**, the proposed PFD comprises five (5) inlets and five (5) outlets. Specifically, the main inlet stream encompasses the feedstock (EFB and MSF), cooling water for heat exchanger operation, the air stream for the ASU, and steam for the WGSR. Conversely, hydrogen constitutes the primary product of the process, while POFA and nitrogen serve as its byproducts. Additionally, the procedure incorporates a flue gas outlet and cooling water.

Hydrogen Purification Process

The product stream from the WGSR contains a notable concentration of contaminants, such as ash, CO, C_2H_6, C_2H_4, and CH_4. Consequently, prior to entry, both the gas separation unit and atmospheric emissions must undergo gas cleaning. Eliminating ash from the system can effectively reduce the load on subsequent equipment and enhance efficiency. Gas cyclones exhibit significant potential for dust removal, typically capable of eliminating around 70 % of particulate matter, sulphur compounds (SOx), and nitrogen oxides (NOx).

To further eradicate any remaining particulate matter in the system, this study proposes the introduction of a gas cyclone upstream of the gas separation unit and downstream of the WGSR. Moreover, the study suggests constructing a gas cyclone with 90 % grade efficiency, which would substantially reduce the presence of particles larger than 0.258 μm. The primary constituent of the ash found in the production facility is known as POFA, which is the residue remaining after the combustion of OPW. Moreover, the extracted POFA could potentially be sold for profit to be utilized in applications such as dense membrane and asphalt [60-62].

Table 22. Detailed deviation comparison table in co-gasification system boundary.

Stream	**41**		
	Aspen	**Excel**	**% Deviation**
Mass flow rate (kg/h)	129087.58	128887.28	0.1552
CO (kg/h)	4504.48	4502.81	0.0371
CO_2 (kg/h)	82312.29	82293.97	0.0223
H_2 (kg/h)	7796.88	7735.46	0.7877
H_2O (kg/h)	30695.39	30669.36	0.0848

Removal of particulate matter is crucial for maintaining clean air quality and adhering to the 2014 Clean Air Regulation [63]. Various technologies are now employed in the CO_2 removal process, including membrane, adsorption, and absorption methods. Membrane separation technologies have been chosen for the hydrogen purification process due to their notable features, which encompass easy operation, minimal capital costs, low energy consumption, and a small environmental footprint.

A review of the literature indicates that metallic membranes utilizing palladium (Pd) demonstrate superior performance in hydrogen permeation recovery, achieving a remarkable 90.5 % recovery rate, along with a 99 % residue recovery rate for CO_2 [56]. Achieving a hydrogen purity of 99 % aligns with the industry standard for purified hydrogen gas. However, it is evident that the membrane's retentate retains a notable amount of residual flue gas. To mitigate greenhouse gas emissions, adhere to the Clean Air Regulation of 2014, and support the Paris Agreement, the implementation of a carbon capture and sequestration (CCS) system or a flue gas treatment system is necessary [63]. This study proposes the adoption of a microalgae-based CO_2 bio-fixation method for flue gas treatment. It is envisaged that the biogas produced through this bio-fixation technology could potentially serve as a fuel source for the production facility [64-66].

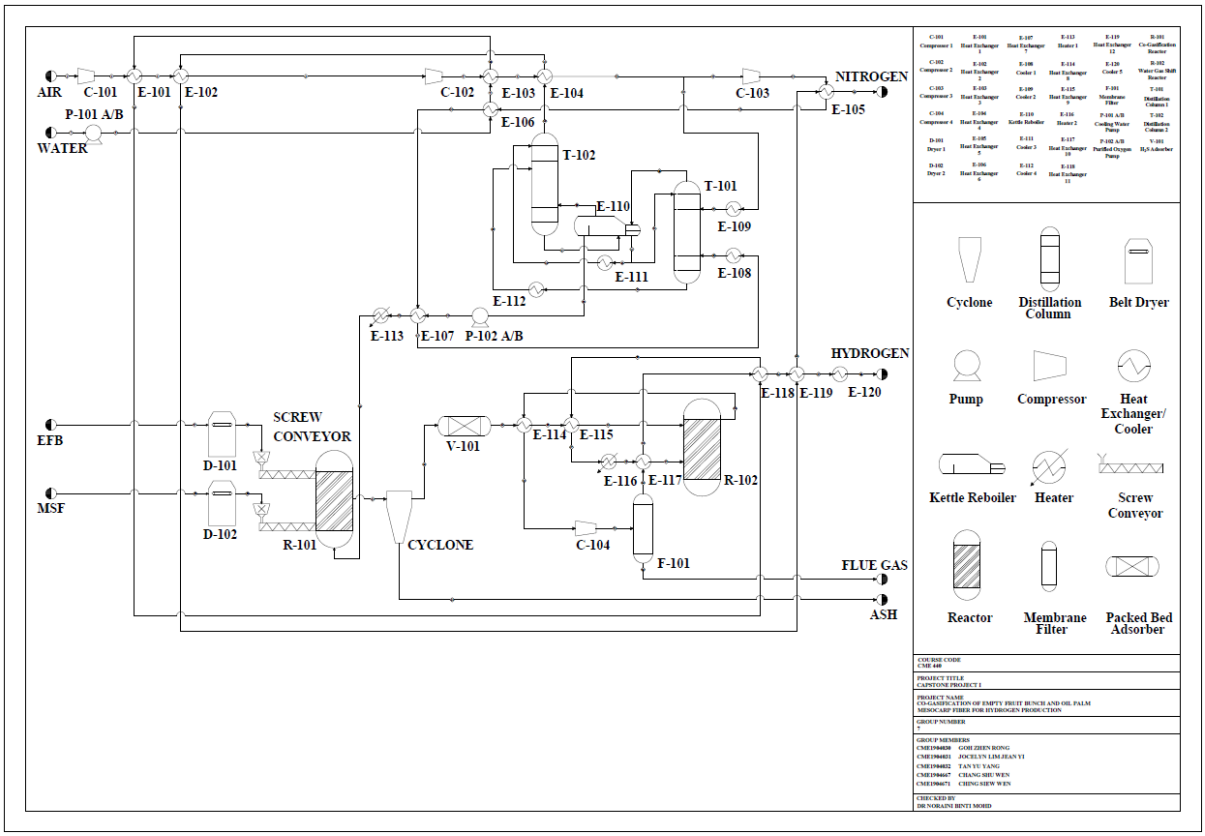

Figure 9. Process flow diagram (PFD): D-101-102 are the belt dryers; R-101-102 are the reactors; E-101-120 are the heat exchangers; V-101 is the packed bed absorber; F-101 is the fluidized bed membrane reactor; C-101-104 are the compressors; P-101-102 A/B are the pumps; T-101-102 are the distillation columns.

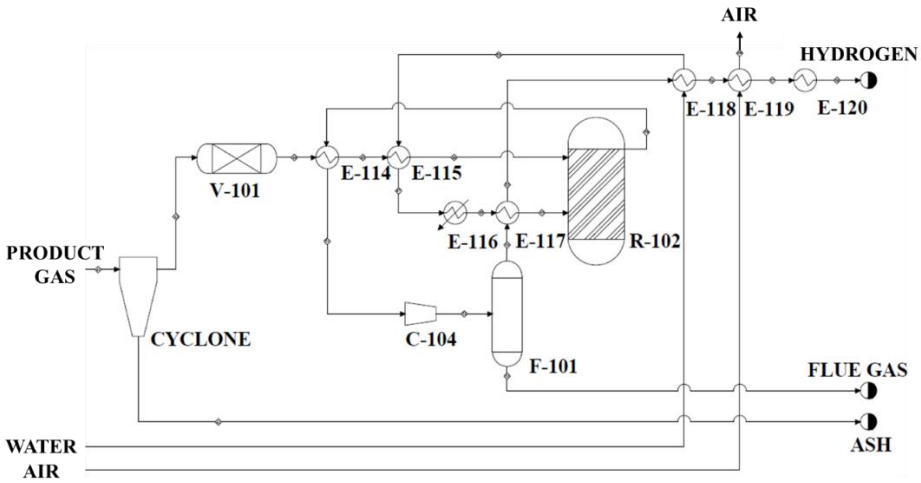

Figure 10. A schematic diagram of the hydrogen purification process: R102 is reactor; V-101 is packed bed adsorber E-114-120 are heat exchangers; F-101 is fluidized bed membrane reactor; C-104 is the compressor.

Integration of Sustainability Elements

Sustainable development, as articulated by the Brundtland Report (1987) and further emphasized by Hajian, underscores the importance of meeting the needs of the present generation without compromising the ability of future generations to meet their own needs. Such initiatives often prioritize long-term sustainability objectives, encompassing social, environmental, and economic considerations [67]. The Triple Bottom Line performance dimensions-financial, environmental, and social-play a pivotal role in advancing

sustainability. In essence, sustainability serves as a framework aimed at enhancing societal well-being and economic prosperity while minimizing adverse impacts on the environment, as noted by Al-Sharrah et al. and Aryanasl et al. [68, 69].

From a holistic perspective, the design of the PFD has integrated sustainability principles spanning economic, social, and environmental dimensions. In essence, leveraging agricultural waste as a precursor for the synthesis of value-added products serves to mitigate environmental pollution by preventing waste accumulation and potential soil contamination resulting from improper disposal practices [70, 71]. Through systematic optimization, efficient utilization of agricultural waste can be achieved, thereby alleviating concerns associated with waste accumulation, reducing greenhouse gas emissions, and fostering environmental conservation. Additionally, the inclusion of flue gas treatment in the plant design aims to minimize greenhouse gas emissions and mitigate air pollution. Moreover, the integration of a gas cyclone in the flue gas cleaning system is geared towards eliminating particulate matter, including POFA. Furthermore, the adoption of a unified cooling water stream to supply heat to the ASU heat exchanger underscores water conservation efforts within the proposed plant design. This approach not only supports water security but also aligns with SDG 6, which addresses clean water and sanitation issues. Furthermore, the plant design envisages a wastewater treatment system, contributing to maritime safety and supporting SDG 14, which focuses on marine life preservation.

From an economic standpoint, the optimization of system operations and design parameters was employed to enhance efficiency and curb energy wastage in crafting the proposed PFD. This optimization strategy aims to foster energy conservation, leading to potential savings in energy expenditure and reducing the overall production costs. Additionally, by minimizing energy consumption and waste, the expenses associated with the final product can be diminished.

Furthermore, in terms of social considerations, the process plant was meticulously planned with safety measures informed by a comprehensive preliminary risk analysis, incorporating preventive and mitigating measures to mitigate the likelihood of accidents. Moreover, the design of the process plant strictly adheres to the guidelines outlined by the Malaysian Department of Occupational Safety and Health, ensuring the health, safety, and welfare of both the community and the workers [72]. To reinforce safety measures, temperature indicators will be installed in the vicinity of the plant, along with pressure relief valves positioned around the co-gasifier and WGSR. Additionally, a robust process control and safety instrumentation system will be implemented to maintain acceptable safety standards.

CONCLUSIONS

In summary, the objectives of this study were successfully achieved. This research advocates for utilizing the co-gasification method to generate hydrogen from biomass sourced from palm trees, considering hydrogen's promising prospects as a clean and efficient alternative to fossil fuels. Projections from market studies indicate a surge in hydrogen demand by 2028, prompting the proposal to establish a facility aimed at producing 62.5 kt of H_2 annually, about half of the targeted market demand [66]. The selection of EFB and MSF as biomass feedstock was driven by their cost-effectiveness, high production rates, and low moisture content. Furthermore, the choice of Kuantan, Pahang (3.8168 ˚N, 103.3317 ˚E) as the site for the gasification plant was based on factors such as suitable land availability, cost-effectiveness, labour supply, transportation accessibility, and infrastructural development. Subsequent to simulating the production process, both material and energy balances were meticulously computed and compared with the simulation's outcomes. Additionally, a comprehensive PFD was crafted. The envisioned outcome is the production of purified hydrogen gas at a rate of around 7000 kg/h, with input rates of EFB and MSF set at 29650 kg/h. An economic assessment estimated the potential cost as USD 12.40 per kg of output.

REFERENCE

1. Alalwan, H. A., Alminshid, A. H. and Aljaafari, H. A. S. (2019) Promising evolution of biofuel generations. Subject review. *Renewable Energy Focus*, **28**, 127–139.

2. Rodionova, M. V., et al. (2022) A comprehensive review on lignocellulosic biomass biorefinery for sustainable biofuel production. *International Journal of Hydrogen Energy*, **47(3)**, 1481–1498.

3. Sarangi, P. K. and Nayak, M. M. (2021) Agro-Waste for Second-Generation Biofuels. *In Liquid Biofuels,* 697–709.

4. Pabbathi, N. P. P., et al. (2023) Role of meta-genomics in prospecting novel endoglucanases, accentuating functional metagenomics approach in second-generation biofuel production: a review. *Biomass Convers Biorefin*, **13(2)**, 1371–1398.

5. Salvador, R., et al., (2021) Key aspects for designing business models for a circular bio-economy. *Journal of Cleaner Production*, **278**, 124341.

6. Ubando, A. T., Felix, C. B. and Chen, W. -H. (2020) Biorefineries in circular bioeconomy: A comprehensive review. *Bioresource Technology*, **299**, 122585.

7. Vural Gursel, I., et al. (2020) Variable demand as

a means to more sustainable biofuels and bio-based materials. *Biofuels, Bioproducts and Biorefining*, **15(1)**, 15–31.

8. Saravanan, A., et al. (2022) Recent advances and sustainable development of biofuels production from lignocellulosic biomass. *Bioresource Technology*, **344**, 126203.

9. Ambaye, T. G., et al. (2021) Emerging technologies for biofuel production: A critical review on recent progress, challenges and perspectives. *J Environ Manage*, **290**, 112627.

10. Fusi, A., et al. (2016) Life Cycle Environmental Impacts of Electricity from Biogas Produced by Anaerobic Digestion. *Frontiers in Bioengineering and Biotechnology*, **4**.

11. Battista, F., et al. (2020) Food wastes and sewage sludge as feedstock for an urban biorefinery producing biofuels and added-value bioproducts. *Journal of Chemical Technology & Biotechnology*, **95(2)**, 328–338.

12. Douglas, J. M. (1985) A hierarchical decision procedure for process synthesis. *AIChE Journal*, **31(3)**, 353–362.

13. Khor, C. S., Madhuranthakam, C. M. R. and Elkamel, A. (2007) Waste Reduction for Chemical Plant Operations. *In Environmentally Conscious Materials and Chemicals Processing*, 89–124.

14. Sinnott, R. K., Coulson, J. M. and Richardson, J. F. (1993) Chemical Engineering Design. *An Introduction to Design (2nd ed.).: Elsevier*, **6**.

15. Dong, J., et al. (2016) Effect of Operating Parameters and Moisture Content on Municipal Solid Waste Pyrolysis and Gasification. *Energy & Fuels*, **30(5)**, 3994–4001.

16. Naryanto, R. F., et al. (2020) The Effect of Moisture Content on the Tar Characteristic of Wood Pellet Feedstock in a Downdraft Gasifier. *Applied Sciences*, **10(8)**.

17. Ding, G. and He, B. (2020) Process Simulation of Co-Gasification of Raw Municipal Solid Waste and Bituminous Coal in CO_2/O_2 Atmosphere. *Applied Sciences*, **10(6)**.

18. Sikarwar, V. S., et al. (2017) Progress in biofuel production from gasification. *Progress in Energy and Combustion Science*, **61**, 189–248.

19. Liao, C., Wu, C. and Yan, Y. (2007) The characteristics of inorganic elements in ashes from a 1 MW CFB biomass gasification power generation plant. *Fuel Processing Technology*, **88(2)**, 149–156.

20. Straka, P. and Bičáková, O. (2014) Hydrogen-rich gas as a product of two-stage co-gasification of lignite/waste plastics mixtures. *International Journal of Hydrogen Energy*, **39(21)**, 10987–10995.

21. Qin, K., et al. (2012) High-temperature entrained flow gasification of biomass. *Fuel*, **93**, 589–600.

22. Rizkiana, J., et al. (2014) Effect of biomass type on the performance of cogasification of low rank coal with biomass at relatively low temperatures. *Fuel*, **134**, 414–419.

23. Belyaev, A. A. (2008) Gasification of low-grade fuels in a spouted bed for power generation. *Solid Fuel Chemistry*, **42(6)**, 335–341.

24. Hafeez, S., et al. (2019) 6 - Catalytic Conversion and Chemical Recovery, in Plastics to Energy, S.M. Al-Salem, Editor. *William Andrew Publishing*, 147–172.

25. Sebastian, J. and Paul, L. (2021) Chapter 13 - Plastic recycling and regeneration, in Sustainable Manufacturing, K. Gupta and K. Salonitis, Editors. *Elsevier*, 339–365.

26. Loha, C., Chatterjee, P. K. and Chattopadhyay, H. (2011) Performance of fluidized bed steam gasification of biomass – Modeling and experiment. *Energy Conversion and Management*, **52(3)**, 1583–1588.

27. Baraj, E., Ciahotný, K. and Hlinčík, T. (2021) The water gas shift reaction: Catalysts and reaction mechanism. *Fuel*, **288,** 119817.

28. Carta, D., et al. (2017) The water gas shift reaction over Pt–CeO_2 nanoparticles confined within mesoporous SBA-16. *Journal of Materials Chemistry A*, **5(37)**, 20024–20034.

29. Chen, C., et al., 2020 Cu/Fe_3O_4 catalyst for water gas shift reaction: Insight into the effect of Fe^{2+} and Fe^{3+} distribution in Fe_3O_4. *International Journal of Hydrogen Energy*, **45(15)**, 8456–8465.

30. Farzanfar, J. and Rezvani, A. R. (2015) Study of a Mn–Cr/TiO2 mixed oxide nanocatalyst prepared via an inorganic precursor complex for high-temperature water–gas shift reaction. *Comptes Rendus Chimie*, **18(2)**, 178–186.

31. Lin, J. -H. and Guliants, V. V. (2012) Alumina-supported Cu@ Ni and Ni@ Cu core–shell nanoparticles: Synthesis, characterization, and catalytic activity in water–gas-shift reaction. *Applied Catalysis A: General*, **445**, 187–194.

32. Amran, M., et al. (2021) Palm Oil Fuel Ash-Based Eco-Efficient Concrete: A Critical Review of the Short-Term Properties. LID - 10.3390/

ma14020332 [doi] LID - 332. *Materials (Print)*, 1996–1944.

33. Yusof, M. S. M., et al. (2020) Arsenic adsorption mechanism on palm oil fuel ash (POFA) powder suspension (Electronic), 1873–3336.

34. Hesketh, J., et al. (2021) Influence of H_2S on the pitting corrosion of 316L stainless steel in oilfield brine. *Corrosion Science*, **182**, 109265.

35. Shah, M. S., Tsapatsis, M. and Siepmann, J. I. (2018) Correction to Hydrogen Sulfide Capture: From Absorption in Polar Liquids to Oxide, Zeolite, and Metal–Organic Framework Adsorbents and Membranes. *Chemical Reviews*, **118(4)**, 2297–2297.

36. Ling, K., Gangoli, V. S. and Barron, A. R. (2019) Synergic Adsorption of H2S Using High Surface Area Iron Oxide–Carbon Composites at Room Temperature. *Energy & Fuels*, **33(8)**, 7509–7521.

37. Mao, J., et al. (2020) Efficient Adsorption of Hydrogen Sulfide at Room Temperature Using Fumed Silica-supported Deep Eutectic Solvents. *Aerosol and Air Quality Research*, **20(1)**, 203–2015.

38. Sigot, L., Ducom, G. and Germain, P. (2016) Adsorption of hydrogen sulfide (H2S) on zeolite (Z): Retention mechanism. *Chemical Engineering Journal*, **287**, 47–53.

39. Ugarte, P., et al. (2017) Dry reforming of biogas in fluidized bed: Process intensification. *International Journal of Hydrogen Energy*, **42(19)**, 13589–13597.

40. Foresti, S., et al. (2018) A comprehensive model of a fluidized bed membrane reactor for small-scale hydrogen production. *Chemical Engineering and Processing - Process Intensification*, **127**, 136–144.

41. Dolan, M., et al. (2016) An experimental and techno-economic assessment of solar reforming for H2 production. *International Journal of Hydrogen Energy*, **41(33)**, 14583–14595.

42. Anzelmo, B., Wilcox, J. and Liguori, S. (2017) Natural gas steam reforming reaction at low temperature and pressure conditions for hydrogen production via Pd/PSS membrane reactor. *Journal of Membrane Science*, **522**, 343–350.

43. Absattarov, A. I., Pisarenko, Y. A. and Mikhailov, M. V. (2019) Pinch Analysis of the Efficiency of a Heat-Exchange System for Styrene Production. *Theoretical Foundations of Chemical Engineering*, **53(4)**, 566–577.

44. Ma, W., Xiang, S. and Xia, L. (2023) Energy-Saving Analysis of Epichlorohydrin Plant Based on Entransy. *Processes*, **11**. DOI: 10.3390/pr 11030954.

45. Mutlu, Ö. Ç. and Zeng, T. (2020) Challenges and Opportunities of Modeling Biomass Gasification in Aspen Plus: A Review. *Chemical Engineering & Technology*, **43(9)**, 1674–1689.

46. Penteado, A. T., et al. (2018) Sequential Flow-sheet Optimization: Maximizing the Exergy Efficiency of a High-Pressure Water Scrubbing Process for Biogas Upgrade. In *Computer Aided Chemical Engineering, A. Friedl, et al., Editors., Elsevier*, 1329–1334.

47. Saali, A., Sakhaeinia, H. and Shokouhi, M. (2021) Modification of Peng–Robinson Cubic Equation of State with Correction of the Temperature Dependency Term. *Journal of Solution Chemistry*, **50(3)**, 402–426.

48. Darmawan, A., et al. (2017) Enhanced Process Integration of Entrained Flow Gasification and Combined Cycle: Modeling and Simulation Using Aspen Plus. *Energy Procedia*, **105**, 303–308.

49. Acar, M. C. and Böke, Y. E. (2018) Simulation of Biomass Gasification Process Using Aspen Plus. In *14th International Combustion Symposium (INCOS2018)*, 134–137.

50. Anyaoha, K. E., et al. (2020) Co-gasification of oil palm biomass in a pilot scale downdraft gasifier. *Energy Reports*, **6**, 1888-1896.

51. Ahmad, I., et al. (2019) Data-Based Prediction and Stochastic Analysis of Entrained Flow Coal Gasification under Uncertainty. *Sensors (Basel)*, **19(7)**.

52. Demirbas, A. (2007) Effect of Temperature on Pyrolysis Products from Biomass. *Energy Sources, Part A: Recovery, Utilization, and Environmental Effects*, **29(4)**, 329–336.

53. Chen, C., et al. (2013) Simulation of municipal solid waste gasification in two different types of fixed bed reactors. *Fuel*, **103**, 58–63.

54. Basile, A., et al. (2015) Water gas shift reaction in membrane reactors: Theoretical investigation by artificial neural networks model and experimental validation. *International Journal of Hydrogen Energy*, **40(17)**, 5897–5906.

55. Faraji, M. and Saidi, M. (2022) Process simulation and optimization of groundnut shell biomass air gasification for hydrogen-enriched syngas production. *International Journal of Hydrogen Energy*, **47(28)**, 13579–13591.

56. Koutsonikolasa, D., K. S. Pantoleontosb, G. and S. G. Zaspalisa, V. (2013) Techno-Economic Assessment of Polymeric, Ceramic and Metallic Membranes Integration in an Advanced IGCC Process for H_2 Production and CO_2 Capture. *Chemical Engineering Transactions*, **35**, 715–720.

57. Querol, E., et al. (2011) Novel application for exergy and thermoeconomic analysis of processes simulated with Aspen Plus®. *Energy*, **36(2)**, 964–974.

58. Gagliano, A., et al. (2017) Development of an Equilibrium-based Model of Gasification of Biomass by Aspen Plus. *Energy Procedia*, **111**, 1010–1019.

59. Phatak, A. A., et al. (2007) Kinetics of the water–gas shift reaction on Pt catalysts supported on alumina and ceria. *Catalysis Today*, **123(1)**, 224–234.

60. Amran, M., et al. (2021) Palm Oil Fuel Ash-Based Eco-Efficient Concrete: A Critical Review of the Short-Term Properties. *Materials (Basel)*, **14(2)**.

61. Thomas, B. S., Kumar, S. and Arel, H. S. (2017) Sustainable concrete containing palm oil fuel ash as a supplementary cementitious material – A review. *Renewable and Sustainable Energy Reviews*, **80**, 550–561.

62. Tai, Z. S., et al. (2018) Low cost palm oil fuel ash based ceramic membranes for oily water separation. *Malaysian Journal of Fundamental and Applied Sciences*, **14(4)**, 419–424.

63. Malaysia, D.O.E. (2014) Clean Air Regulation.

64. Kassim, M. A. and Meng, T. K. (2017) Carbon dioxide (CO_2) biofixation by microalgae and its potential for biorefinery and biofuel production. *Science of The Total Environment*, **584-585**, 1121–1129.

65. Daneshvar, E., et al. (2022) Biologically-mediated carbon capture and utilization by microalgae towards sustainable CO2 biofixation and biomass valorization – A review. *Chemical Engineering Journal*, **427**.

66. Iamtham, S. and Sornchai, P. (2022) Biofixation of CO_2 from a power plant through large-scale cultivation of Spirulina maxima. *South African Journal of Botany*, **147**, 840–851.

67. Hajian, M. and Jangchi Kashani, S. (2021) 1 - Evolution of the concept of sustainability. From Brundtland Report to sustainable development goals. In *Sustainable Resource Management, C.M. Hussain and J.F. Velasco-Muñoz, Editors, Elsevier*, 1–24.

68. Al-Sharrah, G., Elkamel, A. and Almanssoor, A. (2010) Sustainability indicators for decision-making and optimisation in the process industry: The case of the petrochemical industry. *Chemical Engineering Science*, **65(4)**, 1452–1461.

69. Aryanasl, A., et al. (2017) Components of sustainability considerations in management of petrochemical industries. *Environment Monitoring Assessment (Electronic)*, 1573–2959.

70. Adejumo, I. O. and Adebiyi, O. A. (2020) Agricultural solid wastes: Causes, effects, and effective management. *Strategies of Sustainable Solid Waste Management*, **8**.

71. Sharma, P., et al. (2020) Microbial strategies for bio-transforming food waste into resources. *Bioresource Technology*, **299**, 122580.

72. Department of Occupational Safety and Health (1994) M. Regulations under Occupational Safety and Health Act 1994 (Act 514).